



## A self-template synthesis of porous $\text{ZnCo}_2\text{O}_4$ microspheres for high-performance quasi-solid-state asymmetric supercapacitors†

Yansong Gai, Yuanyuan Shang, Liangyu Gong,\* Linghao Su, Long Hao, Fengying Dong and Jianzhong Li

A facile self-template solvothermal method was developed to fabricate a microsphere precursor, which was followed by annealing in air to give  $\text{ZnCo}_2\text{O}_4$  microspheres. The  $\text{ZnCo}_2\text{O}_4$  microspheres possess irregular diameters from 600 nm to 1.2  $\mu\text{m}$  and a high specific surface area of  $34.60 \text{ m}^2 \text{ g}^{-1}$  with an average pore diameter of 6.96 nm. Each  $\text{ZnCo}_2\text{O}_4$  microsphere was found to be constructed by many intertwined nanoparticles. When investigated as electrode materials for supercapacitors, the  $\text{ZnCo}_2\text{O}_4$  microspheres exhibited a high specific capacitance of  $542.5 \text{ F g}^{-1}$  at  $1 \text{ A g}^{-1}$ , excellent rate capability of 55.3% retention at  $10 \text{ A g}^{-1}$ , and good cycling stability with 95.5% retention of the maximum capacitance ( $440 \text{ F g}^{-1}$ ) after 2000 cycles at  $2 \text{ A g}^{-1}$ . Additionally, a quasi-solid-state asymmetric supercapacitor fabricated with the as-prepared  $\text{ZnCo}_2\text{O}_4$  microspheres was used as the positive electrode and activated carbon as the negative electrode. The asymmetric device exhibited a remarkable cycling stability with 76.68% retention of the maximum capacitance ( $68.93 \text{ F g}^{-1}$ ) after 1000 cycles at  $0.5 \text{ A g}^{-1}$ . Moreover, two asymmetric devices connected in a series can successfully light up a red light-emitting-diode (LED) and last for more than 15 min. Therefore, this fascinating electrochemical performance demonstrates that the  $\text{ZnCo}_2\text{O}_4$  microspheres have potential applications in supercapacitors.

Received 28th October 2016  
Accepted 20th November 2016

DOI: 10.1039/c6ra25950b  
[www.rsc.org/advances](http://www.rsc.org/advances)

### Introduction

With rapid social development and improvement in human lifestyle, the demands for renewable and sustainable energy have continued to increase. To fulfill these energy requirements, significant attention has been given to energy storage devices.<sup>1,2</sup> Supercapacitors, an alternative to batteries and traditional electrostatic capacitors, are considered as one of the most promising and reliable devices in the field of energy storage due to their fast recharge ability, high power performance, long lifespan, low maintenance cost, and environmental friendliness.<sup>3–5</sup> These advantages are crucial for their applications in systems, such as hybrid electric vehicles, high power portable electronics, and backup energy systems, that require a quick release of energy.<sup>6</sup> Based on the underlying energy storage mechanism, supercapacitors can be classified into electrical double layer capacitors (EDLCs) and pseudocapacitors.<sup>7–9</sup> EDLCs store energy *via* the accumulation of electrostatic charge at the surface of carbonaceous materials, whereas pseudocapacitors utilize fast and reversible surface or near-surface reactions for charge storage.<sup>10–12</sup> Compared to

EDLCs, pseudocapacitors can provide substantially higher capacitance and energy density due to their multiple oxidation states.<sup>13</sup> Therefore, numerous efforts have been dedicated to develop pseudocapacitance materials, including metal oxides, hydroxides and sulphides, in the past few years.<sup>14–19</sup>

Transition metal oxides are emerging as the most promising electrode materials for pseudocapacitors due to their excellent intrinsic properties, such as high theoretical specific capacitance, low cost, and environmentally friendly nature. Typical transition metal oxides, such as  $\text{NiO}$ ,  $\text{ZnO}$ ,  $\text{MnO}_2$ ,  $\text{Co}_3\text{O}_4$ ,  $\text{Fe}_2\text{O}_3$ , and  $\text{TiO}_2$  have been extensively studied as pseudocapacitive electrode materials.<sup>15,20–24</sup> However, poor intrinsic electrical conductivity, slow ion diffusion rates and poor electrochemical stability of these materials restrict their widespread applications as high-performance supercapacitor electrodes.<sup>25</sup> To address this issue and improve the electrochemical performance, mixed transition metal oxides, such as  $\text{NiCo}_2\text{O}_4$ ,<sup>26</sup>  $\text{CuCo}_2\text{O}_4$ ,<sup>27</sup>  $\text{NiMoO}_4$ ,<sup>28</sup>  $\text{CoMoO}_4$ ,<sup>11</sup> and  $\text{CoMn}_2\text{O}_4$ ,<sup>29</sup> have drawn increasing attention for new type of pseudocapacitive materials with outstanding performance due to their many unique properties, which originate from the coexistence of two different cations in a single crystal structure. Compared to single metal oxides, mixed transition metal oxides exhibit high theoretical capacitance, good electronic conductivity, and rich redox reactions due to their multiple oxidation states, which are beneficial for a significant enhancement in the electrochemical

College of Chemistry and Pharmaceutical Sciences, Qingdao Agricultural University, Qingdao 266109, PR China. E-mail: lygong@163.com

† Electronic supplementary information (ESI) available. See DOI: 10.1039/c6ra25950b



performance when used as pseudocapacitive materials.<sup>12,30,31</sup>  $\text{ZnCo}_2\text{O}_4$  is a typical mixed transition metal oxide with cubic spinel structure. The bivalent Zn ions occupy one eighth of the tetrahedral sites in the cubic spinel structure, and the trivalent Co ions occupy one half of the octahedral sites in the face-centered cubic oxygen lattice.<sup>2,32</sup> To date, various types of  $\text{ZnCo}_2\text{O}_4$  nanostructures, such as nanowires,<sup>2</sup> nanoflowers,<sup>33</sup> nanorods,<sup>34</sup> and microspheres,<sup>35,36</sup> have been prepared. Because of their large specific surface area and uniform pore size distribution, mesoporous microspheres are still under the focus of recent research as potential and appealing electrode materials to prepare high-performance supercapacitors. Mesoporous microspheres can largely increase the amount of electroactive sites and provide extra free space to effectively alleviate the structural strain that occurs during the charge–discharge process, which is beneficial for a significant enhancement in the electrochemical performance in terms of high reversible capacity and outstanding cyclability.<sup>35,37</sup>

Herein, we present a two-step facile strategy involving a hydrothermal method and subsequent thermal annealing treatment to fabricate  $\text{ZnCo}_2\text{O}_4$  microspheres. The obtained  $\text{ZnCo}_2\text{O}_4$  microspheres exhibit a high specific surface area and good electronic conductivity. When evaluated as electrode materials for supercapacitors, the  $\text{ZnCo}_2\text{O}_4$  microspheres show a high specific capacity of  $542.5 \text{ F g}^{-1}$  at  $1 \text{ A g}^{-1}$ , as well as good cycle stability. Furthermore, a quasi-solid-state asymmetric supercapacitor was fabricated with the as-prepared  $\text{ZnCo}_2\text{O}_4$  microspheres as the positive electrode and activated carbon as the negative electrode. Two asymmetric devices connected in a series can successfully light up a red light-emitting-diode (LED), which lasts for more than 15 min. These results show that the  $\text{ZnCo}_2\text{O}_4$  microspheres have great potential for applications in high-performance energy storage devices.

## Experimental

### Synthesis of $\text{ZnCo}_2\text{O}_4$ microspheres

All chemical reagents were of analytical purity and were used without further purification. In a typical procedure, 1 mmol of  $\text{Co}(\text{Ac})_2 \cdot 4\text{H}_2\text{O}$ , 0.5 mmol of  $\text{Zn}(\text{Ac})_2 \cdot 4\text{H}_2\text{O}$ , and 12 mL of diethylene glycol (DEG) were dissolved in a 60 mL of isopropanol. Then, the solution was transferred to a Teflon-lined stainless steel autoclave and heated at  $200^\circ\text{C}$  for 10 h. After naturally cooling down to room temperature, the resulting precipitates were collected by centrifugation, washed several times with absolute ethanol and dried at  $80^\circ\text{C}$  in an oven. To obtain different interior structures of the  $\text{ZnCo}_2\text{O}_4$  microspheres, the precipitates were calcined at  $450^\circ\text{C}$  for 2 h at various ramp rates.

### Characterization

The crystallographic structures of the samples were examined by X-ray diffraction (XRD, Cu  $\text{K}\alpha$  radiation,  $\lambda = 1.5406 \text{ \AA}$ ) using a Bruker D8 advanced X-ray Diffractometer. The morphology and intrinsic structure were examined using scanning electron microscopy (SEM, JEOL 7500F) and transmission electron

microscope (TEM, JEOL-2010). The nitrogen adsorption/desorption isotherms were characterized at 77 K on a Quantachrome NOVA2200e analyzer. The specific surface area was calculated using the Brunauer–Emmett–Teller (BET) method, whereas the pore size distribution was calculated from the adsorption branch isotherms using the Barrette–Joyner–Halenda (BJH) method.

### Electrochemical measurements

The working electrode was fabricated by compressing a mixture of active material, conductive material (acetylene black), and binder (polytetrafluoroethylene (PTFE)) in a weight ratio of  $\text{ZnCo}_2\text{O}_4/\text{acetylene black/PTFE}$  of  $8:1:1$  onto a nickel foam current collector. Electrochemical measurements were conducted using a three-electrode system in  $6 \text{ mol L}^{-1}$  KOH at room temperature, where a platinum plate and a saturated calomel electrode (SCE) were used as the counter and reference electrodes, respectively. Cyclic voltammetry (CV) and electrochemical impedance spectroscopy (EIS) measurements were performed using a CHI660D electrochemical workstation (Chenhua, Shanghai, China). Galvanostatic charge–discharge (GCD) tests were evaluated using a Land CT2001A battery program control test system (LAND, Wuhan, China).

### Assembly of the $\text{ZnCo}_2\text{O}_4/\text{ACs}$ quasi-solid-state asymmetric supercapacitor

A solid-state asymmetric capacitor was assembled using the as-prepared  $\text{ZnCo}_2\text{O}_4$  electrode as the positive electrode, active carbon (AC) as the negative electrode with a separator and PVA/KOH gel as a solid electrolyte. The negative electrode was prepared by mixing active carbon and PTFE in a mass ratio of  $9:1$ . The PVA/KOH gel electrolyte was prepared by mixing 5.6 g KOH and 6 g PVA in 60 mL of deionized water, which was then heated at  $85^\circ\text{C}$  with stirring until the solution became clear. Two pieces of the electrode and the separator (cellulose PP/PE) were immersed in the gel for 5 min, and then taken out and assembled together. After solidification at room temperature, the asymmetrical capacitor was obtained. The related calculation involved is given in the ESI.†

## Results and discussion

As an important intermediate for porous  $\text{ZnCo}_2\text{O}_4$ ,  $\text{ZnCo}_2\text{O}_4$  precursor was characterized by FT-IR spectroscopy and XRD. As shown in Fig. 1A, the IR spectrum of the precursor shows a strong broad peak at  $3450 \text{ cm}^{-1}$  due to the stretching vibration of OH. The weak peaks at  $2974$  and  $2931 \text{ cm}^{-1}$  are ascribed to the stretching vibration of the C–H group. The peaks at around  $1623$  and  $1137 \text{ cm}^{-1}$  are attributed to the vibration of C–O and C–O–C groups, respectively, whereas the broad peak at  $1420 \text{ cm}^{-1}$  could be ascribed to the interlayer acetate ( $\text{CH}_3\text{COO}^-$ ). In addition, the peak at  $487 \text{ cm}^{-1}$  could be attributed to the vibration of the M–O group (M : Zn or Co).<sup>38</sup> Fig. 1C shows the XRD pattern of the  $\text{ZnCo}_2\text{O}_4$  precursor, and the diffraction peaks are consistent with the  $\text{ZnO}$  phase (JPCDS card no. 36-1451). In addition, an obvious diffraction peak at approximately  $12^\circ$  can



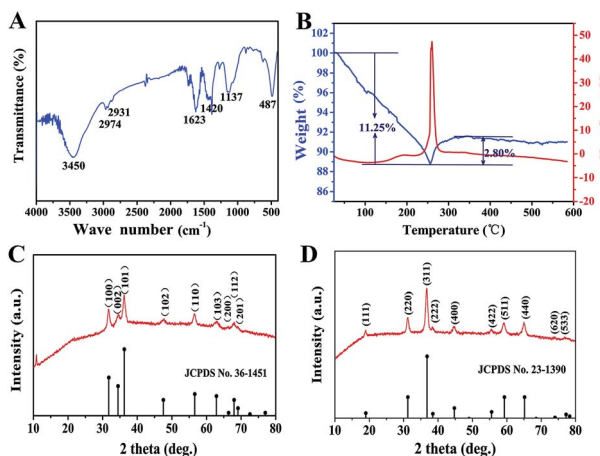


Fig. 1 (A) The FT-IR spectrum of the ZnCo-precursor. (B) The TG and DTA curves obtained for the ZnCo-precursor. (C) The XRD pattern of the ZnCo-precursor. (D) The XRD pattern of ZnCo<sub>2</sub>O<sub>4</sub>.

be observed, which is characteristic of metal glycolates or alkoxide derivatives.<sup>39</sup> Combining the FT-IR spectroscopy results, ZnCo-precursor is proposed as a mixture of ZnO and M-O-CH<sub>2</sub>-CH<sub>2</sub>-O-CH<sub>2</sub>-CH<sub>2</sub>-O-M (M: Co, Zn or H).

To understand the calcination process of the as-prepared ZnCo-precursor, DTA-TG analysis was performed and the result is shown in Fig. 1B. The continuous weight loss of *ca.* 11.25% at temperature ranging from room temperature to 256 °C may be attributed to the dehydration and decomposition of the organic species in the ZnCo-precursor. Then, the weight exhibited a rebound of *ca.* 2.80% around 256–350 °C and a highly exothermic peak appeared at 260 °C.<sup>38</sup> This phenomenon can be attributed to the combustion of organic species in the ZnCo-precursor. Moreover, the ZnCo-precursor was converted to ZnCo<sub>2</sub>O<sub>4</sub>. The slight weight loss occurred around 350–450 °C was attributed to the continuous combustion of the organic residues. There was almost no quality loss after 450 °C; thus, we selected the temperature of 450 °C for the calcination of the ZnCo-precursor to ensure its complete decomposition. The ZnCo<sub>2</sub>O<sub>4</sub> products were studied by XRD analysis to identify its purity and crystallographic structure. As shown in Fig. 2D, all the diffraction peaks after calcination can be unambiguously assigned to cubic ZnCo<sub>2</sub>O<sub>4</sub> (JCPDS card no. 23-1390) and no other phases or impurities were detected, indicating the high purity of the sample. Based on the Scherrer formula ( $D = 0.89/\lambda B \cos \theta$ ) and XRD data, an average crystalline size of 14.68 nm was estimated from the (311) peak (the strongest peak).

The morphology and architecture of the ZnCo<sub>2</sub>O<sub>4</sub> products were carefully observed by means of SEM and HRTEM. The typical SEM images of the pure ZnCo<sub>2</sub>O<sub>4</sub> products (Fig. 2A) show that they are composed of monodisperse microspheres with irregular diameters ranging from 600 nm to 1.2 μm. The higher magnification SEM image (Fig. 2B) shows that the surface of the ZnCo<sub>2</sub>O<sub>4</sub> microspheres was very rough and comprised small nanoparticles. The TEM image of the ZnCo<sub>2</sub>O<sub>4</sub> product (Fig. 2C) also shows that it is comprised of monodisperse and completely solid spheres with irregular diameters. The enlarged TEM image (Fig. 2D) clearly shows that there are numerous

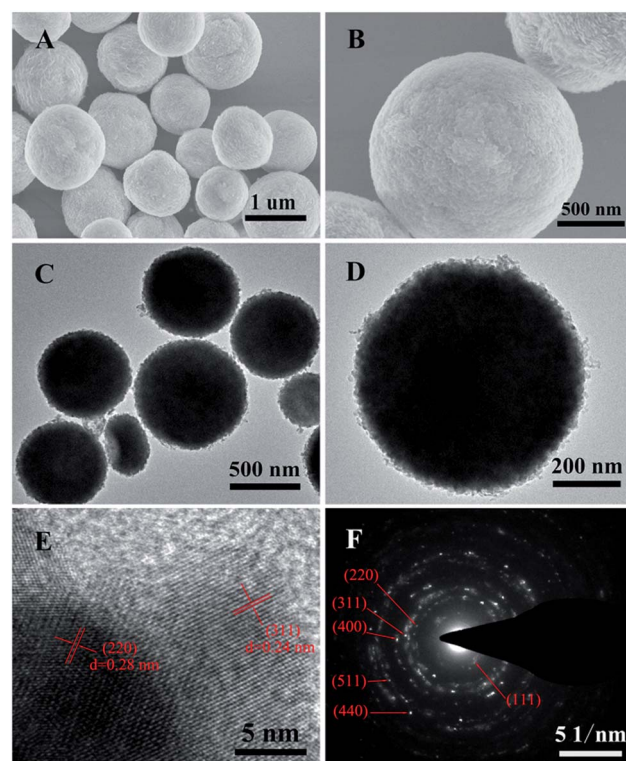


Fig. 2 (A and B) SEM images, (C and D) TEM images, (E) HRTEM image and (F) the corresponding SAED pattern of the ZnCo<sub>2</sub>O<sub>4</sub> microspheres.

nanoparticles closely packed on the edges of the microspheres, which is in good agreement with the SEM observations. A further HRTEM image of the ZnCo<sub>2</sub>O<sub>4</sub> microspheres is shown in Fig. 3E. Interplanar spacings of about 0.28 nm and 0.24 nm can be observed, corresponding to the (220) and (311) planes, respectively. The corresponding selected-area electron diffraction (SAED) pattern of the ZnCo<sub>2</sub>O<sub>4</sub> microspheres in Fig. 5F shows well-defined diffraction rings, and the diffraction rings can be readily indexed to the (111), (220), (311), (400), (511), and (440) planes of the ZnCo<sub>2</sub>O<sub>4</sub> phase, which is consistent with the results of abovementioned analysis.

To better elucidate the reaction mechanism responsible for the formation of the microsphere precursors, a series of time-dependent experiments were carried out. The morphologies of the products after the solvothermal treatment for different time intervals were characterized by SEM. As shown in Fig. 3A, a mass of irregular bulks was formed after 2 h of reaction and they were aggregated together. When the reaction was continued for 4 h, the irregular morphology of the bulk material turned into spheroidal (Fig. 3B). As the reaction time was prolonged to 6 h, they gradually blossom into regular microspheres; however, the microspheres were still aggregated together (Fig. 3C). When the reaction time was further prolonged to 8 h, monodisperse microspheres were obtained and lots of nanorods were closely packed on their surface (Fig. 3D). Finally, the uniform and well-rounded microspheres precursors were obtained when the reaction duration was extended to 10 h (Fig. 3E). A close SEM examination (Fig. 3F) reveals that these microsphere precursors were composed of closely packed

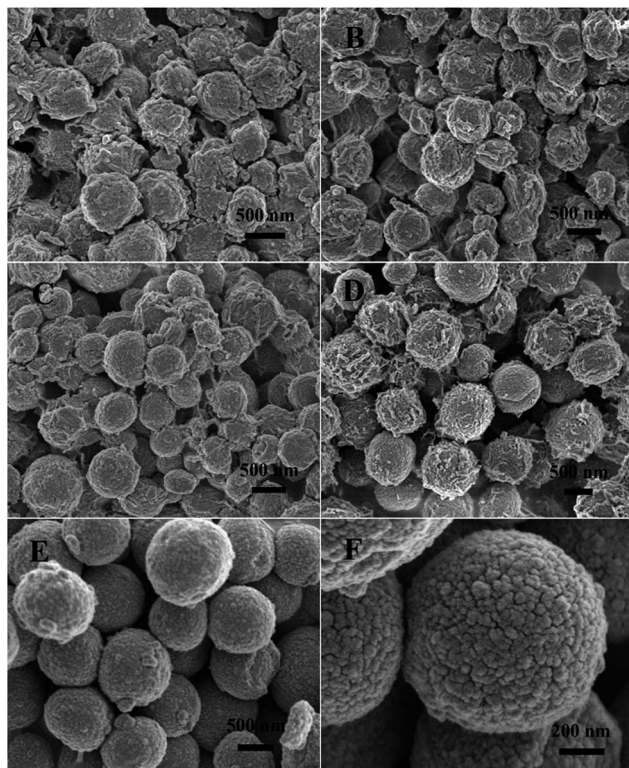
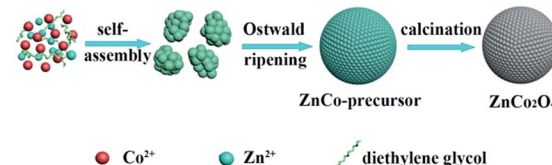


Fig. 3 SEM images of the ZnCo-precursor prepared under different growth conditions: (A) 2 h, (B) 4 h, (C) 6 h, (D) 8 h, and (E and F) 10 h.

nano-particles, and the neighboring particles connected together to create a rough and porous structure.

Based on the abovementioned experimental observations, a plausible formation mechanism is summarized in Scheme 1. During the initial nucleation and crystal growth stage, a large number of nanoparticles form and tend to gather together to form spheroidal agglomerates driven by the minimization of interfacial energy.<sup>39-41</sup> Then, the spheroidal agglomerate serves as a center to adsorb the newly formed nanoparticles. Moreover, the adsorbed nanoparticles with a higher surface energy and a smaller size dissolve and transfer to the spheroidal agglomerates due to the Ostwald ripening process.<sup>40</sup> As the Ostwald ripening process continues, the spheroidal agglomerates become robust and well-rounded. Finally, well-defined microsphere precursors are formed. After calcination in air, the precursors are completely converted to ZnCo<sub>2</sub>O<sub>4</sub> and the morphology of the precursors is well preserved. Due to the decomposition of the organic species in the calcination process, the porosity is effectively improved.

The porosity of the ZnCo<sub>2</sub>O<sub>4</sub> microspheres was further investigated using BET measurements. As shown in Fig. 4A, the N<sub>2</sub> adsorption-desorption isotherm obtained for ZnCo<sub>2</sub>O<sub>4</sub> exhibits a type-IV isotherm with a H3 hysteresis loop, indicating the presence of a mesoporous structure. The corresponding pore size distribution confirmed by the BJH method is shown in Fig. 4B. The pore size distribution was mainly centered in the range of 2–10 nm with an average pore diameter of 6.96 nm. Moreover, the BET specific surface area and total pore volume of



Scheme 1 Schematic of the formation process of the ZnCo<sub>2</sub>O<sub>4</sub> microspheres.

the ZnCo<sub>2</sub>O<sub>4</sub> sample were calculated to be 34.60 m<sup>2</sup> g<sup>-1</sup> and 0.11 cm<sup>3</sup> g<sup>-1</sup>, respectively. The high specific surface area with suitable mesopore distribution is beneficial for the fast diffusion of the electrolyte and can facilitate ion diffusion at the electrode–electrolyte interface during the electrochemical processes. Therefore, this kind of mesoporous structure is believed to enhance the properties of the supercapacitors.

The electrochemical performance of ZnCo<sub>2</sub>O<sub>4</sub> was measured by cyclic voltammetry (CV), galvanostatic charge–discharge (GCD), and electrochemical impedance spectroscopy (EIS) measurements in 6.0 M aqueous KOH electrolyte using a three-electrode electrochemical cell. Fig. 5A shows the CV curves obtained for the ZnCo<sub>2</sub>O<sub>4</sub> electrode in a potential range of −0.2–0.5 V at scan rates ranging from 5 to 100 mV s<sup>-1</sup>. The shape of all CV curves exhibit a pair of well-defined redox peaks, which mainly originate from the reversible faradaic redox reactions related to M–O/M–O–OH (M refers to Co and Zn ions) associated with OH<sup>−</sup> anions, confirming the pseudocapacitive characteristics.<sup>42,43</sup> Furthermore, the shape of the CV curves can be well maintained when the potential scan rates are varied from 5 to 100 mV s<sup>-1</sup>, demonstrating the excellent rate capability and improved mass transport of the electrode.<sup>44</sup> Note that, the cathodic and anodic peaks shift towards lower and higher potential with increase in the scan rates, respectively, which can be attributed to the internal resistance and polarization effect during the faradaic process.<sup>25,45</sup> However, the position of the cathodic or anodic peaks only slightly shift, which suggests the good reversibility and the fast charge/discharge response of the ZnCo<sub>2</sub>O<sub>4</sub> electrode.<sup>46</sup>

Fig. 5B presents the GCD curves obtained for the ZnCo<sub>2</sub>O<sub>4</sub> electrode with a potential window ranging from 0 to 0.4 V at various current densities ranging from 1 to 10 A g<sup>-1</sup>. The pseudocapacitive behavior was further confirmed by the non-linear charge/discharge profile. It can be observed that there are voltage plateaus during the charge/discharge

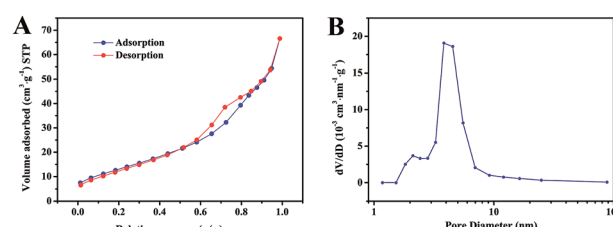


Fig. 4 (A) The nitrogen adsorption and desorption isotherm and (B) corresponding BJH pore size distribution of the ZnCo<sub>2</sub>O<sub>4</sub> microspheres.



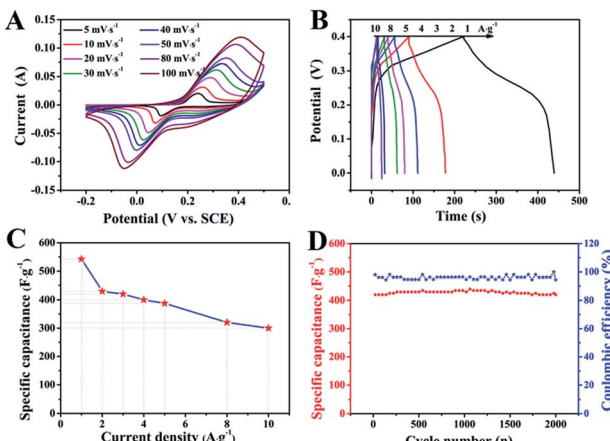


Fig. 5 The electrochemical test results of the  $\text{ZnCo}_2\text{O}_4$  microsphere electrode. (A) The CV curves at various scan rates. (B) The GCD curves at various current density. (C) The capacitance as a function of current density. (D) The cycling performance and Coulomb efficiency at  $2 \text{ A g}^{-1}$ .

measurements, which are consistent with the CV curves. The calculated specific capacitance based on the discharge curves as a function of the current density is plotted in Fig. 5C. The  $\text{ZnCo}_2\text{O}_4$  electrode delivers a high pseudocapacitance of  $542.5, 430, 420, 400, 387.5, 320$ , and  $300 \text{ F g}^{-1}$  at current densities of  $1, 2, 3, 4, 5, 8$ , and  $10 \text{ A g}^{-1}$ , respectively. Along with the increase in current density, the corresponding specific capacitances gradually decrease, which can be attributed to the low diffusion of electrolyte ion and the presence of inner active sites that are unable to completely sustain the redox transitions.<sup>47</sup> About 55.3% of the capacitance of the  $\text{ZnCo}_2\text{O}_4$  electrode was retained when the current density was increased from  $1$  to  $10 \text{ A g}^{-1}$ , which demonstrates an outstanding rate capability and superior electrochemical capacitance. In addition, the cycling stability was also evaluated by the repeated charge–discharge measurements at a constant current density of  $2 \text{ A g}^{-1}$  for 2000 cycles, as shown in Fig. 5D. Clearly, about 95.5% of the maximum capacitance ( $440 \text{ F g}^{-1}$ ) was retained after 2000 continuous charge–discharge cycles, showing an excellent cyclic stability. The coulombic efficiency during the 2000 charge–discharge cycles was more than 98%, which confirmed the electrochemical suitability of the  $\text{ZnCo}_2\text{O}_4$  electrode, whose redox reactions are quite feasible. The electrochemical impedance spectroscopy (EIS) measurements (Fig. S1, ESI†) indicate the high electrical conductivity, low internal resistance, and fast charge transportation of the  $\text{ZnCo}_2\text{O}_4$  microspheres, which may be helpful for the excellent rate capability.

To evaluate the potential applications of our  $\text{ZnCo}_2\text{O}_4$  microspheres, we assembled a quasi-solid-state asymmetric supercapacitor device based on the  $\text{ZnCo}_2\text{O}_4$  microsphere electrode as the anode, ACs on Ni foam as the cathode, KOH–PVA gel as the solid electrolyte and a piece of cellulose paper as the separator as shown in Fig. 6A. Fig. 6B shows the CV curves obtained for the fabricated  $\text{ZnCo}_2\text{O}_4/\text{AC}$  asymmetric supercapacitor at different voltage windows obtained at a scan rate of  $10 \text{ mV s}^{-1}$ . The CV curves were stable even at  $1.4 \text{ V}$ . However, when the potential was higher than  $1.4 \text{ V}$ , the CV curves

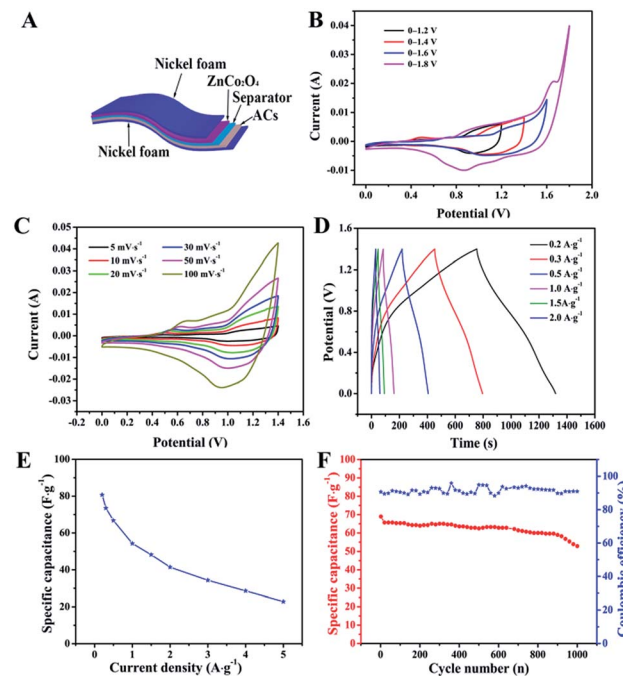


Fig. 6 (A) A schematic of the  $\text{ZnCo}_2\text{O}_4/\text{AC}$  quasi-solid-state asymmetric supercapacitor. (B) CV curves obtained at different potential windows. (C) The CV curves obtained at various scan rates. (D) The GCD attributed to some irreversible reactions occurring in the potential curves under different current densities. (E) The specific capacitance of the device as a function of current density. (F) The cycling performance and the corresponding Coulomb efficiency at  $0.5 \text{ A g}^{-1}$ .

exhibited a distortion and a slight hump that can be attributed to some irreversible reactions occurring when the potential window was higher than  $1.4 \text{ V}$ .<sup>48</sup> Therefore,  $1.4 \text{ V}$  was used as the default voltage value for further investigation. Fig. 6C displays the CV curves of the quasi-solid-state asymmetric supercapacitor at various scan rates from  $2$  to  $100 \text{ mV s}^{-1}$ . As the scan rate increased, the closed areas of the CV curves were augmentative, whereas the shapes were well retained, implying the fast charge–discharge performance of the asymmetric device. The GCD curves of the quasi-solid-state asymmetric supercapacitor at a set of current densities from  $0.1 \text{ A g}^{-1}$  to  $2 \text{ A g}^{-1}$  are illustrated in Fig. 6D. It was observed that all the GCD curves were nearly symmetric, indicating an excellent electrochemical reversibility and good coulombic efficiency. Based on the total masses of the two electrodes, the calculated specific capacitance of the asymmetric device as a function of the current densities was plotted and is shown in Fig. 6E. The specific capacitance of the asymmetric device was  $80.71, 66.78, 54.28, 41.42$ , and  $22.86 \text{ F g}^{-1}$  at current densities of  $0.2, 0.5, 1.0, 2.0$ , and  $5.0 \text{ A g}^{-1}$ , respectively. The cycle performance and coulombic efficiency of the quasi-solid-state asymmetric supercapacitor were carried out at  $0.5 \text{ A g}^{-1}$  for 1000 cycles, as shown in Fig. 6F. After 1000 cycles, the specific capacitance of the quasi-solid-state asymmetric supercapacitor was  $52.86 \text{ F g}^{-1}$  with about 76.68% of the initial capacitance being retained. Furthermore, the coulombic efficiency was maintained at about 91% during the consecutive cycles.



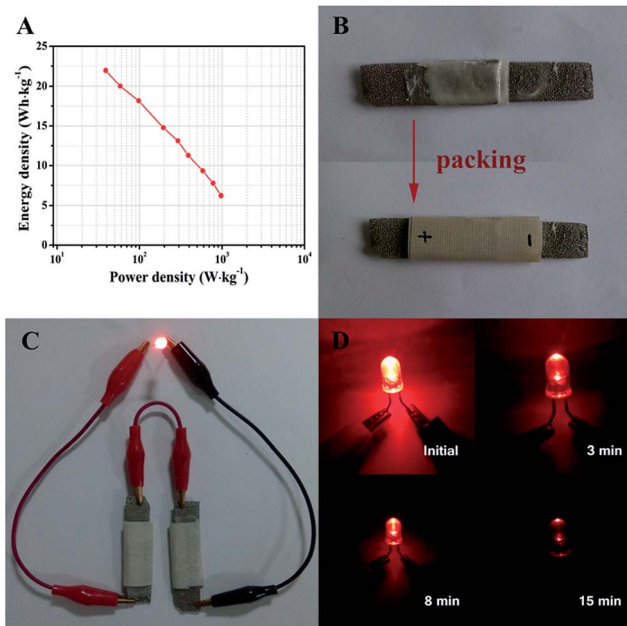


Fig. 7 (A) Ragone plots of the  $\text{ZnCo}_2\text{O}_4/\text{AC}$  quasi-solid-state asymmetric supercapacitor. (B) Digital photographs of the  $\text{ZnCo}_2\text{O}_4/\text{AC}$  quasi-solid-state asymmetric supercapacitor before and after packing. (C) Optical images of a red LED powered by two solid-state asymmetric supercapacitors connected in a series. (D) The evaluation of the lightened red LED at different stages after corresponding to (C).

Ragone plots of the  $\text{ZnCo}_2\text{O}_4/\text{AC}$  quasi-solid-state asymmetric supercapacitor device derived from the charge–discharge measurements at different current densities are presented in Fig. 7A. The quasi-solid-state asymmetric supercapacitor can provide a maximum energy density of  $21.97 \text{ W h kg}^{-1}$  at a power density of  $38.89 \text{ W kg}^{-1}$ , which still remains  $6.22 \text{ W h kg}^{-1}$  at a high power density of  $972.22 \text{ W kg}^{-1}$ . Furthermore, the as-fabricated  $\text{ZnCo}_2\text{O}_4/\text{AC}$  quasi-solid-state asymmetric supercapacitor was packed with PTFE tape to form a device, as shown in Fig. 7B. In addition, two solid-state asymmetric supercapacitors connected in a series can light up a 5 mm diameter red ( $2.0 \text{ V}, 20 \text{ mA}$ ) round light-emitting diode (LED), which lasts for more than 15 min (Fig. 7C and D) and indicates the excellent practical application potential of the devices as an energy storage system.

## Conclusions

In summary, porous  $\text{ZnCo}_2\text{O}_4$  microspheres have been successfully fabricated using a facile hydrothermal method followed by a calcination process. It exhibits excellent electrochemical performance with a high specific capacitance of  $542.5 \text{ F g}^{-1}$  at  $1 \text{ A g}^{-1}$ , a remarkable long-term cycling stability (95.5% of the maximum capacitance is retained after 2000 cycles at  $2 \text{ A g}^{-1}$ ), good reversibility features, and an excellent rate capability. In addition, an all solid-state asymmetric supercapacitor was successfully fabricated with outstanding cycling life, in which the specific capacitance was maintained at about 76.68% of the initial capacitance. The all solid-state asymmetric supercapacitor can light up a red LED that lasts

for more than 15 min, endowing our quasi-solid-state asymmetric supercapacitor new opportunities as energy storage devices for various electronic systems. Our results bode well for the practical application of  $\text{ZnCo}_2\text{O}_4$  microspheres materials in future high-performance supercapacitors.

## Acknowledgements

This work was financially supported by the Natural Science Foundation of China (NSFC (21404066 and 51603114)), the Shandong Province Natural Science Foundation (ZR2014DP003 and ZR2016EMQ03), the Outstanding Young Scientists Incentive foundation of Shandong Province (BS2010NJ007), and the Science and Technology Foundation of Qingdao City (Grant No. 16-5-1-43-jch).

## Notes and references

- Z. Gao, W. Yang, J. Wang, N. Song and X. Li, *Nano Energy*, 2015, **13**, 306–317.
- B. Guan, D. Guo, L. Hu, G. Zhang, T. Fu, W. Ren, J. Li and Q. Li, *J. Mater. Chem. A*, 2014, **2**, 16116–16123.
- D. P. Dubal, O. Ayyad, V. Ruiz and P. Gomez-Romero, *Chem. Soc. Rev.*, 2015, **44**, 1777–1790.
- C. Zheng, C. Cao, R. Chang, J. Hou and H. Zhai, *Phys. Chem. Chem. Phys.*, 2016, **18**, 6268–6274.
- R. R. Salunkhe, J. Tang, Y. Kamachi, T. Nakato, J. H. Kim and Y. Yamauchi, *ACS Nano*, 2015, **9**, 6288–6296.
- H. Chen, J. Jiang, Y. Zhao, L. Zhang, D. Guo and D. Xia, *J. Mater. Chem. A*, 2015, **3**, 428–437.
- R. R. Salunkhe, Y. H. Lee, K. H. Chang, J. M. Li, P. Simon, J. Tang, N. L. Torad, C. C. Hu and Y. Yamauchi, *Chemistry*, 2014, **20**, 13838–13852.
- J. Tang and Y. Yamauchi, *Nat. Chem.*, 2016, **8**, 638–639.
- J. Tang, R. R. Salunkhe, J. Liu, N. L. Torad, M. Imura, S. Furukawa and Y. Yamauchi, *J. Am. Chem. Soc.*, 2015, **137**, 1572–1580.
- X. Zheng, Y. Ye, Q. Yang, B. Geng and X. Zhang, *Dalton Trans.*, 2016, **45**, 572–578.
- L. An, W. Li, Y. Cao, K. Xu, R. Zou, T. Ji, L. Yu and J. Hu, *Dalton Trans.*, 2015, **44**, 21131–21140.
- D. Cheng, Y. Yang, J. Xie, C. Fang, G. Zhang and J. Xiong, *J. Mater. Chem. A*, 2015, **3**, 14348–14357.
- S. Gao, F. Liao, S. Ma, L. Zhu and M. Shao, *J. Mater. Chem. A*, 2015, **3**, 16520–16527.
- S. Hou, G. Zhang, W. Zeng, J. Zhu, F. Gong, F. Li and H. Duan, *ACS Appl. Mater. Interfaces*, 2014, **6**, 13564–13570.
- B. Zhu, S. Tang, S. Vongehr, H. Xie and X. Meng, *ACS Appl. Mater. Interfaces*, 2016, **8**, 4762–4770.
- L. Huang, D. Chen, Y. Ding, Z. L. Wang, Z. Zeng and M. Liu, *ACS Appl. Mater. Interfaces*, 2013, **5**, 11159–11162.
- M. Li, S. Xu, Y. Zhu, P. Yang, L. Wang and P. K. Chu, *J. Alloys Compd.*, 2014, **589**, 364–371.
- S. Peng, L. Li, H. Tan, R. Cai, W. Shi, C. Li, S. G. Mhaisalkar, M. Srinivasan, S. Ramakrishna and Q. Yan, *Adv. Funct. Mater.*, 2014, **24**, 2155–2162.



19 J.-C. Xing, Y.-L. Zhu, Q.-W. Zhou, X.-D. Zheng and Q.-J. Jiao, *Electrochim. Acta*, 2014, **136**, 550–556.

20 X. Ren, C. Guo, L. Xu, T. Li, L. Hou and Y. Wei, *ACS Appl. Mater. Interfaces*, 2015, **7**, 19930–19940.

21 P. Yang, X. Xiao, Y. Li, Y. Ding, P. Qiang, X. Tan, W. Mai, Z. Lin, W. Wu, T. Li, H. Jin, P. Liu, J. Zhou, C. P. Wong and Z. LinWang, *ACS Nano*, 2013, **7**, 2617–2626.

22 Z. Chen, C. X. Kronawitter and B. E. Koel, *Phys. Chem. Chem. Phys.*, 2015, **17**, 29387–29393.

23 S. Yang, X. Song, P. Zhang and L. Gao, *ACS Appl. Mater. Interfaces*, 2015, **7**, 75–79.

24 X. Lu, G. Wang, T. Zhai, M. Yu, J. Gan, Y. Tong and Y. Li, *Nano Lett.*, 2012, **12**, 1690–1696.

25 H. Niu, X. Yang, H. Jiang, D. Zhou, X. Li, T. Zhang, J. Liu, Q. Wang and F. Qu, *J. Mater. Chem. A*, 2015, **3**, 24082–24094.

26 L. Shen, L. Yu, X. Y. Yu, X. Zhang and X. W. Lou, *Angew. Chem.*, 2015, **54**, 1868–1872.

27 M. Kuang, X. Y. Liu, F. Dong and Y. X. Zhang, *J. Mater. Chem. A*, 2015, **3**, 21528–21536.

28 S. Peng, L. Li, H. B. Wu, S. Madhavi and X. W. D. Lou, *Adv. Energy Mater.*, 2015, **5**, 1401172.

29 G. Gao, S. Lu, Y. Xiang, B. Dong, W. Yan and S. Ding, *Dalton Trans.*, 2015, **44**, 18737–18742.

30 H. Chen, J. Jiang, L. Zhang, T. Qi, D. Xia and H. Wan, *J. Power Sources*, 2014, **248**, 28–36.

31 S. Chen, M. Xue, Y. Li, Y. Pan, L. Zhu and S. Qiu, *J. Mater. Chem. A*, 2015, **3**, 20145–20152.

32 C. Wu, J. Cai, Q. Zhang, X. Zhou, Y. Zhu, L. Li, P. Shen and K. Zhang, *Electrochim. Acta*, 2015, **169**, 202–209.

33 W. Bai, H. Tong, Z. Gao, S. Yue, S. Xing, S. Dong, L. Shen, J. He, X. Zhang and Y. Liang, *J. Mater. Chem. A*, 2015, **3**, 21891–21898.

34 B. Liu, B. Liu, Q. Wang, X. Wang, Q. Xiang, D. Chen and G. Shen, *ACS Appl. Mater. Interfaces*, 2013, **5**, 10011–10017.

35 H. Chen, Q. Zhang, J. Wang, Q. Wang, X. Zhou, X. Li, Y. Yang and K. Zhang, *Nano Energy*, 2014, **10**, 245–258.

36 L. Huang, G. H. Waller, Y. Ding, D. Chen, D. Ding, P. Xi, Z. L. Wang and M. Liu, *Nano Energy*, 2015, **11**, 64–70.

37 M. S. Park, J. Kim, K. J. Kim, J. W. Lee, J. H. Kim and Y. Yamauchi, *Phys. Chem. Chem. Phys.*, 2015, **17**, 30963–30977.

38 Y. Wang, J. Ke, Y. Zhang and Y. Huang, *J. Mater. Chem. A*, 2015, **3**, 24303–24308.

39 L. Hu, H. Zhong, X. Zheng, Y. Huang, P. Zhang and Q. Chen, *Sci. Rep.*, 2012, **2**, 986.

40 S. Peng, Y. Hu, L. Li, X. Han, F. Cheng, M. Srinivasan, Q. Yan, S. Ramakrishna and J. Chen, *Nano Energy*, 2015, **13**, 718–726.

41 L. Liu, H. Zhang, J. Yang, Y. Mu and Y. Wang, *J. Mater. Chem. A*, 2015, **3**, 22393–22403.

42 G. Q. Zhang, H. B. Wu, H. E. Hoster, M. B. Chan-Park and X. W. Lou, *Energy Environ. Sci.*, 2012, **5**, 9453.

43 W. Yang, Z. Gao, J. Ma, X. Zhang, J. Wang and J. Liu, *J. Mater. Chem. A*, 2014, **2**, 1448–1457.

44 J. Wang, X. Zhang, Q. Wei, H. Lv, Y. Tian, Z. Tong, X. Liu, J. Hao, H. Qu, J. Zhao, Y. Li and L. Mai, *Nano Energy*, 2016, **19**, 222–233.

45 S. Gu, Z. Lou, X. Ma and G. Shen, *ChemElectroChem*, 2015, **2**, 1042–1047.

46 Y. Zhu, Z. Wu, M. Jing, X. Yang, W. Song and X. Ji, *J. Power Sources*, 2015, **273**, 584–590.

47 H. Chen, J. Jiang, L. Zhang, H. Wan, T. Qi and D. Xia, *Nanoscale*, 2013, **5**, 8879–8883.

48 X. Wang, C. Yan, A. Sumboja and P. S. Lee, *Nano Energy*, 2014, **3**, 119–126.

